

Article

Structure, Luminescence and Temperature Detection Capability of $[\text{C}(\text{NH}_2)_3]\text{M}(\text{HCOO})_3$ ($\text{M} = \text{Mg}^{2+}, \text{Mn}^{2+}, \text{Zn}^{2+}$) Hybrid Organic–Inorganic Formate Perovskites Containing Cr^{3+} Ions

Dagmara Stefańska * , Adam Kabański, Thi Hong Quan Vu , Marek Adaszyński  and Maciej Ptak 

Włodzimierz Trzebiatowski Institute of Low Temperature and Structure Research, Polish Academy of Sciences, 50-422 Wrocław, Poland; a.kabanski@intibs.pl (A.K.); q.vu@intibs.pl (T.H.Q.V.); m.adaszynski@intibs.pl (M.A.); m.ptak@intibs.pl (M.P.)

* Correspondence: d.stefanska@intibs.pl

Abstract: Metal-organic frameworks are of great interest to scientists from various fields. This group also includes organic–inorganic hybrids with a perovskite structure. Recently their structural, phonon, and luminescent properties have been paid much attention. However, a new way of characterization of these materials has become luminescence thermometry. Herein, we report the structure, luminescence, and temperature detection ability of formate organic–inorganic perovskite $[\text{C}(\text{NH}_2)_3]\text{M}(\text{HCOO})_3$ ($\text{Mg}^{2+}, \text{Mn}^{2+}, \text{Zn}^{2+}$) doped with Cr^{3+} ions. Crystal field strength (Dq/B) and Racah parameters were determined based on diffuse reflectance spectra. It was shown that Cr^{3+} ions are positioned in the intermediate crystal field or close to it with a Dq/B range of 2.29–2.41. The co-existence of the spin-forbidden and spin-allowed transitions of Cr^{3+} ions enable the proposal of an approach for remote readout of the temperature. The relative sensitivity (S_r) can be easily modified by sample composition and Cr^{3+} ions concentration. The luminescent thermometer based on the ${}^2\text{E}/{}^4\text{T}_{2g}$ transitions has the relative sensitivity S_r of $2.08\%K^{-1}$ at 90 K for $[\text{C}(\text{NH}_2)_3]\text{Mg}(\text{HCOO})_3$: 1% Cr^{3+} and decrease to $1.20\%K^{-1}$ at 100 K and $1.08\%K^{-1}$ at 90 K for Mn^{2+} and Zn^{2+} analogs, respectively.

Keywords: MOF; hybrid perovskite; luminescence; thermometry; chromium(III) ions; temperature sensing



Citation: Stefańska, D.; Kabański, A.; Vu, T.H.Q.; Adaszyński, M.; Ptak, M. Structure, Luminescence and Temperature Detection Capability of $[\text{C}(\text{NH}_2)_3]\text{M}(\text{HCOO})_3$ ($\text{M} = \text{Mg}^{2+}, \text{Mn}^{2+}, \text{Zn}^{2+}$) Hybrid Organic–Inorganic Formate Perovskites Containing Cr^{3+} Ions. *Sensors* **2023**, *23*, 6259. <https://doi.org/10.3390/s23146259>

Academic Editors: Liwang Liu, Ping Lu and Yovan de Coene

Received: 30 May 2023

Revised: 6 July 2023

Accepted: 7 July 2023

Published: 9 July 2023



Copyright: © 2023 by the authors. Licensee MDPI, Basel, Switzerland. This article is an open access article distributed under the terms and conditions of the Creative Commons Attribution (CC BY) license (<https://creativecommons.org/licenses/by/4.0/>).

1. Introduction

The noticeable development of hybrid organic–inorganic perovskites (HOIPs) has been observed in recent years. The materials with the general formula ABX_3 , where A is an inorganic or organic cation (e.g., NH_4^+ , $(\text{CH}_3)_2\text{NH}^+$), B is a divalent metal ion (e.g., Pb^{2+} , Zn^{2+}), and X a monovalent anion (e.g., Cl^- , HCOO^-) have attracted increasing attention due to their extraordinary properties [1–3]. Hybrid materials, e.g., $\text{CH}_3\text{NH}_3\text{PbCl}_3$, have been particularly implemented in state-of-the-art photovoltaic devices [4–6]. However, their potential usefulness is significantly greater due to their characteristics, including ferroelectricity [7,8], magnetic [9], optoelectronic [4], and luminescent properties [10–13]. The characteristics of investigated materials can be widely tuned by the replacement of A, B, and X linkers [10,14].

Among various materials, the perovskite-like metal-organic frameworks (MOFs) containing formate anions (HCOO^-) exhibit unique features, such as ferroelectricity, multiferroicity, and luminescence [1,10,15]. Particularly, the group of Cr-based materials shows strong luminescence and weak concentration quenching [2,10,15]. Nevertheless, temperature-dependent luminescence is one of the most outstanding phenomena. The temperature change induces the change in energy level populations, which makes formate-based compounds containing Cr^{3+} ions sufficient materials for non-contact temperature sensing [10].

The optical properties of the transition metals (TM), including chromium trivalent ions, can be affected by the crystal field (CF) strength [13,14,16]. The change in the CF strength

leads to the change in the dominant transition type [17]. The Cr^{3+} ions luminescence may contain two particular emission bands: narrow spin-forbidden ${}^2\text{E}_g \rightarrow {}^4\text{A}_{2g}$ (around 700 nm) and broad spin-allowed ${}^4\text{T}_{2g} \rightarrow {}^4\text{A}_{2g}$ (around 750 nm). In low temperatures, the narrow ${}^2\text{E}_g \rightarrow {}^4\text{A}_{2g}$ emission is dominant. The increase in temperature induces the thermal population of the ${}^4\text{T}_{2g}$ level and, consequently, promotes the broad ${}^4\text{T}_{2g} \rightarrow {}^4\text{A}_{2g}$ emission. The narrow emission takes place in a strong CF environment. The spin-allowed emission, in turn, occurs in a weak crystal field strength. The coexistence of both types of emission indicates the intermediate CF strength. The progressive increase in temperature leads to luminescence quenching. The significant influence of temperature on spectroscopic characteristics of Cr^{3+} -based materials has become the basis of the thermometric model development [10,13].

Luminescence temperature sensing has attracted increasing attention recently [10,18–22]. Non-contact thermometry has great potential for application in scientific, industrial, and biomedical areas [23,24]. Among various advantages, the high accuracy and single measurement speed are noteworthy. The possibility of the plunge measurements going beyond typical thermal imaging limitations makes this approach a promising tool for industrial process monitoring [10].

Temperature sensing is mainly based on the detectable change in the luminescent properties induced by the change in the temperature. A thermometric model can be developed by monitoring changes in lifetime, peak position, as well as the insensitivities of specific peaks [20,25]. The comparison of the intensities of two temperature-dependent emission bands allows us to determine a thermometric parameter called fluorescence intensity ratio (FIR or Δ). Such an approach is called the ratiometric method and has been the most frequently reported application recently [18]. The methods relying on FIR analysis provide high sensitivity and make it possible to implement the independent sensing ranges, which leaves room for model optimization [13,26].

The vast majority of reported thermometric compounds are based on inorganic host materials with rare-earth (RE) elements as dopants [11,25,27,28]. However, the materials containing transition metal ions exhibit promising thermometric characteristics comparable to the solutions based on RE ions [29,30]. The highly sensitive thermometric properties have been reported, inter alia, for the perovskite materials containing ethylammonium cation and Cr^{3+} ions [10]. The development of luminescent thermometers based solely on chromium trivalent ions is a noteworthy approach enabling to deviate from the RE-based materials. Another notable strategy for the development of the ratiometric thermometer, presented in this work, is not only considering the luminescence of Cr^{3+} ions but also using the luminescence of the amine group, such as guanidinium cation ($[\text{C}(\text{NH}_2)_3]^+$ denoted as GA^+). The multicomponent thermometric model may be a promising approach toward higher sensitivity.

Herein, we report the synthesis as well as the structural and spectroscopic properties of the first metal–organic framework luminescent thermometers based on both GA^+ and Cr^{3+} ion luminescence. Investigated series of $[\text{GA}]\text{M}_{1-x}\text{Cr}_x(\text{HCOO})_3$, where $\text{M} = \text{Mg}^{2+}$, Mn^{2+} , Zn^{2+} , and $x = 0, 0.01, 0.03, 0.05$, have been synthesized and investigated as promising thermometric materials. The selection of three distinct cations was motivated by the fact that Mn^{2+} ions are the only ones that are optically active, and Zn^{2+} and Mg^{2+} ions create structures with different properties compared to transition metal ions such as Mn^{2+} . All series exhibit outstanding temperature-dependent emission, which has become the basis of the thermometric analysis. This work is an attempt to describe the effect of the material composition on the luminescent properties with particular emphasis on luminescent thermometry. The optimization of the sensing range estimation is particularly considered.

2. Materials and Methods

The starting materials include formic acid HCOOH (POCH, $\geq 98\%$), ethanol $\text{C}_2\text{H}_5\text{OH}$ (POCH, 96%), guanidine carbonate salt $[\text{GA}][\text{C}(\text{NH}_2)_3]_2\text{CO}_3$, (Sigma Aldrich, 99%) (Sigma Aldrich, Saint Louis, MI, USA), zinc(II) chloride ZnCl_2 (Sigma Aldrich, 99.999%) (Sigma Aldrich, Saint Louis, USA), manganese(II) perchlorate hydrate $\text{Mn}(\text{ClO}_4)_2 \cdot 6\text{H}_2\text{O}$ (Sigma

Aldrich, $\geq 99\%$) (Sigma Aldrich, Saint Louis, USA), magnesium(II) chloride anhydrous MgCl_2 (Sigma Aldrich, 99.9%), and chromium(III) chloride CrCl_3 (Sigma Aldrich, 99%). All precursors were commercially available and were used for the synthesis without any further purification. In this study, a series of $[\text{GA}]M_{1-x}\text{Cr}_x(\text{HCOO})_3$ where $M = \text{Mn, Mg, Zn}$, and $x = 0, 1\%, 3\%, 5\%$, were obtained by using the low-diffusion synthesis method. To grow $[\text{GA}]M_{1-x}\text{Cr}_x(\text{HCOO})_3$ crystals, at first formic acid (8.7 mmol) and GA (4.2 mmol) was dissolved in distilled water (20 mL). This solution was added by an aqueous solution (10 mL) containing 1.0 mmol of $\text{Mn}(\text{ClO}_4)_2 \cdot 6\text{H}_2\text{O}/\text{ZnCl}_2/\text{MgCl}_2$ for the pure samples. The amount of Cr^{3+} ions was calculated based on the molarity of the M^{2+} ions (see Tables S1–S3). The resulting mixed solution was kept undisturbed and allowed to evaporate slowly. After two weeks, the crystals were harvested, washed with ethanol, and dried in the air. The color of the crystals was light pink for Mn or white for Mg and Zn. It also varied from green to dark green depending on the concentration of Cr^{3+} ions.

The powder X-ray diffraction (XRD) patterns were obtained on an X'Pert Pro X-ray diffraction system (Malvern Panalytical, Malvern, UK) equipped with a PIXcel detector (Malvern Panalytical, Malvern, UK) and using $\text{CuK}\alpha$ radiation ($\lambda = 1.54056 \text{ \AA}$). The Raman spectra were measured using a Bruker FT 110/S (Billerica, MA, USA) spectrometer operating at 1064 nm (Nd:YAG). The spectra were collected in a spectral range of $75\text{--}3200 \text{ cm}^{-1}$ and with a spectral resolution of 2 cm^{-1} . The diffuse reflectance spectra were obtained using a Varian Cary 5E UV–VIS–NIR spectrometer (Varian, Palo Alto, CA, USA). The temperature-dependent emission spectra were obtained with a Hamamatsu PMA-12 (Hamamatsu Photonics, Iwata, Japan) photonic multichannel analyzer combined with a BT-CCD sensor. As an excitation source, a 405 nm laser diode was used. The temperature was controlled by a Linkam THMS600 stage (Linkam, Tadworth, UK).

3. Results and Discussion

3.1. Structural Properties

The phase purity of all samples was confirmed by the XRD patterns with a simulation of the single-crystal structural data of $[\text{GA}]M_{1-x}\text{Cr}_x(\text{HCOO})_3$ (Figure 1). The samples with Mn^{2+} and Zn^{2+} crystallized in the orthorhombic $Pnma$ crystal structure [31], and the details of the crystal structure of analogs with Mg^{2+} remain unknown. In general, the formate in-connected MnO_6 framework crates cavities occupied by GA^+ cations (see Figure 2). The right-shifting of the diffraction lines was observed due to the partial replacement of Mn^{2+} (CR = 81 \AA), Mg^{2+} (CR = 86 \AA), and Zn^{2+} ions (CR = 88 \AA) by Cr^{3+} ions (CR = 75.5 \AA). The crystal radius (CR) was obtained from Shannon [32]. No additional phases were detected, which indicates that the Cr^{3+} ions were substituted by the cation M.

The Raman spectra of the $[\text{GA}]M_{1-x}\text{Cr}_x(\text{HCOO})_3$ series, where $M = \text{Mg}^{2+}, \text{Mn}^{2+}, \text{Zn}^{2+}$, and $x = 0, 0.01, 0.03, 0.05$, are marked in Figure 3a as GAMg, GAMn, and GAZn, respectively. All spectra are very similar and are consistent with the reported orthorhombic $Pnma$ symmetry of all crystals [31,33–35]. However, some differences can be seen in the band shifts and the number of components, which are due to the different sizes, masses, and electronegativity of the metal cations that build the crystals. All these parameters affect the sizes of unit cells, causing Raman bands for $[\text{GA}]M(\text{HCOO})_3$ ($M = \text{Mg}^{2+}, \text{Mn}^{2+}, \text{Zn}^{2+}$) to be shifted relative to each other (Figure 3b,c and Table S4). Regarding $[\text{GA}]\text{Zn}(\text{HCOO})_3$, the upshifts observed for $[\text{GA}]\text{Mg}(\text{HCOO})_3$ are most pronounced for lattice modes observed below 300 cm^{-1} since they are very sensitive to the long-range order in the crystal. In addition, strong shifts towards higher wavenumbers, up to 12.3 cm^{-1} for $[\text{GA}]\text{Mg}(\text{HCOO})_3$ and 10.3 cm^{-1} for $[\text{GA}]\text{Mg}(\text{HCOO})_3$, are also observed for NH stretching vibrations above 2850 cm^{-1} (Figure 3d), which further indicate the weakest hydrogen bonds in the $[\text{GA}]\text{Mg}(\text{HCOO})_3$ crystal and stronger for $[\text{GA}]\text{Zn}(\text{HCOO})_3$. The upshift of 7.1 cm^{-1} when Zn^{2+} ions are replaced by Mg^{2+} was evidenced by bands associated with vibrations of oxygen atoms directly coordinated by metal ions, i.e., $\nu_2 + \nu_5$ that have been assigned to symmetric C–O stretching vibrations coinciding with C–H in-plane bending modes, respectively (Figure 3b) [36]. A much weaker upshift is observed for the stretching

C–N modes, reaching 3.1 cm^{-1} for $[\text{GA}]\text{Mg}(\text{HCOO})_3$ and 3.2 cm^{-1} for $[\text{GA}]\text{Mn}(\text{HCOO})_3$ related to $[\text{GA}]\text{Zn}(\text{HCOO})_3$ (Figure 3a). This finding indicates very similar confinement of GA^+ cations and similar dynamics in the perovskite void for $\text{M} = \text{Mg}^{2+}$ and Mn^{2+} .

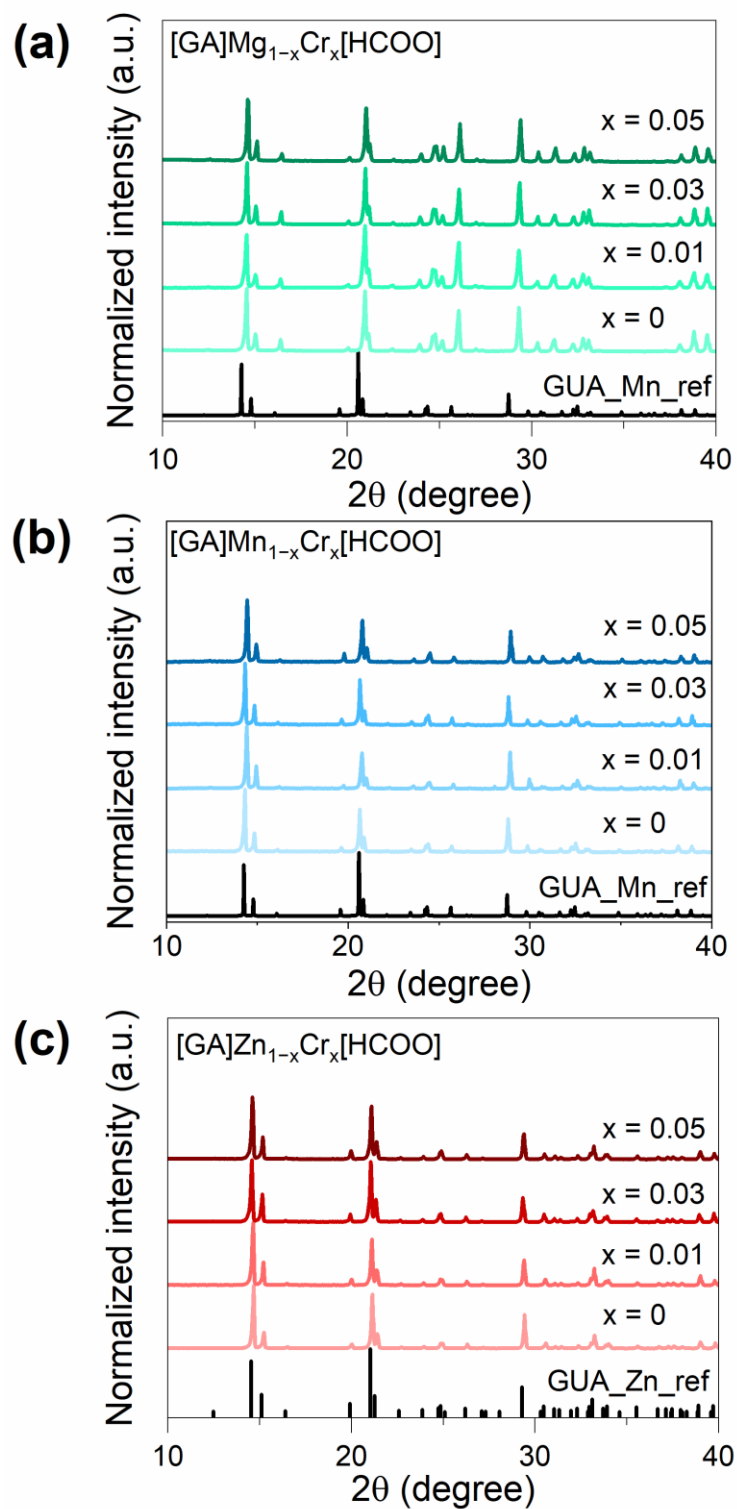


Figure 1. XRD patterns for a series of $[\text{GA}]\text{Mg}_{1-x}\text{Cr}_x(\text{HCOO})_3$ ($x = 0, 0.01, 0.03, 0.05$) (a), $[\text{GA}]\text{Mn}_{1-x}\text{Cr}_x(\text{HCOO})_3$ ($x = 0, 0.01, 0.03, 0.05$) (b), and $[\text{GA}]\text{Zn}_{1-x}\text{Cr}_x(\text{HCOO})_3$ ($x = 0, 0.01, 0.03, 0.05$) (c).

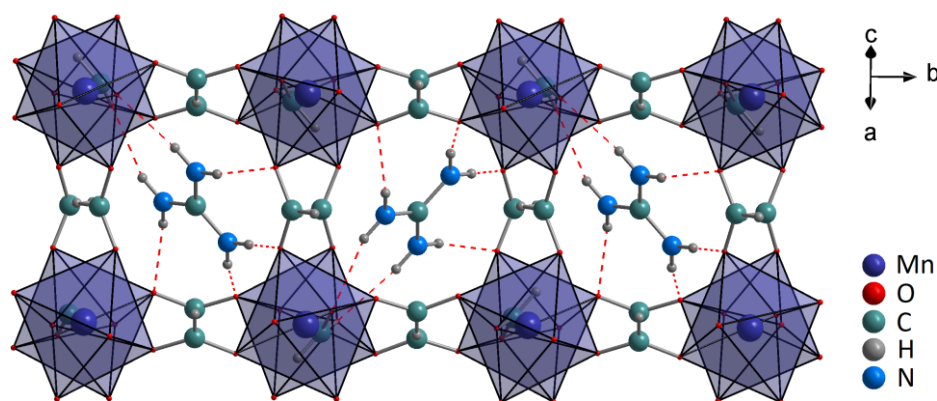


Figure 2. The crystal structure of $[\text{GA}]\text{Mn}(\text{HCOO})_3$ based on data presented in [31]. The dashed lines present HBs between GA^+ cations and the manganese-formate framework.

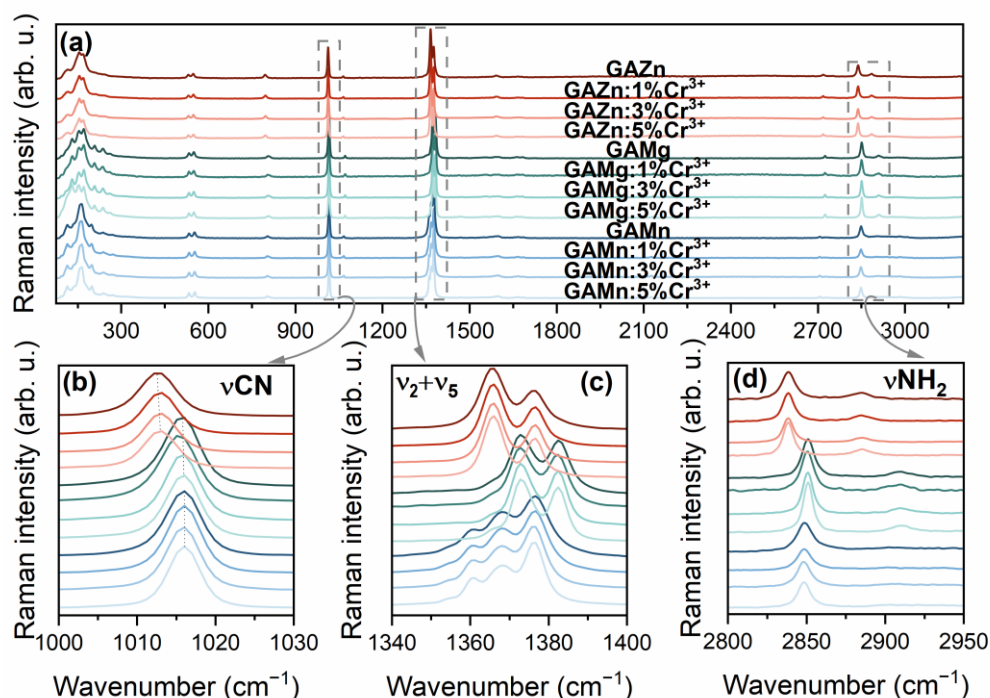


Figure 3. The Raman spectra of the $[\text{GA}]\text{M}_{1-x}\text{Cr}_x(\text{HCOO})_3$ series, where $\text{M} = \text{Mg}^{2+}$, Mn^{2+} , Zn^{2+} , and $x = 0, 0.01, 0.03$, and 0.05 (a) and the enlarged areas with bands corresponding to stretching C–N (b), symmetric C–O stretching and C–H in-plane bending ($\nu_2 + \nu_5$) (c), and stretching N–H modes (d).

The introduction of Cr^{3+} ions into the crystal structure of $[\text{GA}]\text{M}(\text{HCOO})_3$ ($\text{M} = \text{Mg}^{2+}$, Mn^{2+} , Zn^{2+}) at such low concentrations causes very subtle effects on the spectra, not exceeding 1 cm^{-1} . This confirms that aliovalent doping up to 5 mol% does not cause significant structural changes in the orthorhombic $Pnna$ structure.

3.2. Optical Properties and Temperature Detection

The diffuse reflectance spectra (DRS) of representative samples $[\text{GA}]\text{M}_{1-x}\text{Cr}_x(\text{HCOO})_3$, where $\text{M} = \text{Mg}^{2+}$, Mn^{2+} , Zn^{2+} , and $x = 0.05$, are shown in Figure 4. The intensity of the DRS spectrum is influenced by many factors, such as the size and position of crystallites [10]. Therefore, the DRS is used only for characterizing the localization of the energy levels of Cr^{3+} ions in each compound and the effect of the concentration of Cr^{3+} ions on the spectrum's shape. Two primary broad bands localized around $16,828 \text{ cm}^{-1}$ (594 nm) and $22,522 \text{ cm}^{-1}$ (444 nm) for Zn-samples, $17,130 \text{ cm}^{-1}$ (583.8 nm) and $23,162 \text{ cm}^{-1}$ (431.7 nm) for Mg-samples, $17,050 \text{ cm}^{-1}$ (586.5 nm) and $23,162 \text{ cm}^{-1}$ (431.7 nm) for Mn-samples can

be distinguished in Figure 3. These two bands are assigned to the spin-allowed transitions ${}^4A_{2g} \rightarrow {}^4T_{1g}$ and ${}^4A_{2g} \rightarrow {}^4T_{2g}$ of Cr^{3+} ions. In addition, a very weak and sharp peak centered at approximately $14,550\text{ cm}^{-1}$ (687.3 nm) is associated with the spin-forbidden transition from the ${}^4A_{2g}$ ground state to the 2E excited level. It was found that when the concentration of Cr^{3+} increases, the position of the ${}^4A_{2g} \rightarrow {}^2E$ lines slightly changes (Figures S1 and S2). However, for the Zn-compounds, the ${}^4A_{2g} \rightarrow {}^2E$ absorption peak is invisible (Figure S3).

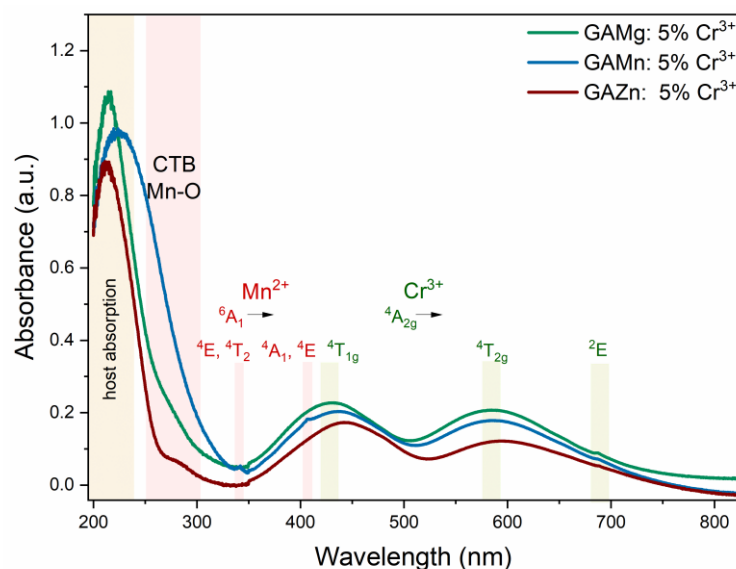


Figure 4. Diffuse reflectance spectra of representative samples $[GA]M_{1-x}Cr_x(HCOO)_3$ ($M = Mg^{2+}$, Zn^{2+} , Mn^{2+} and $x = 0.05$) measured at 300 K.

Noticeably, in the spectrum of Mn-samples, very weak and sharp peaks appeared at $29,240\text{ cm}^{-1}$ (342 nm) and $24,570\text{ cm}^{-1}$ (407 nm), which are attributed to the absorption of Mn^{2+} ions from 6A_1 ground state to 4E , 4T_2 , and 4A_1 , 4E excited levels, respectively. The intensity of these bands decreases as the content of Cr^{3+} increases (Figures S1–S3).

In addition, the intense band located at around $46,729\text{ cm}^{-1}$ (214 nm) can be assigned to host absorption, and it moved to $44,643\text{ cm}^{-1}$ (224 nm) for the Mn-based sample. What is more, the band is much broader because of overlapping with the Mn-O charge transfer band (CTB) (Figure S4).

The crystal field Dq , Racah, B , and C parameters were calculated for Cr^{3+} -doped samples (see Table 1) by using the same methodology as presented in reference [10]. Crystal field strength (CFS) Dq/B parameter is in the range of 2.29–2.39 for GAMn and 2.23–2.41 for GAMg samples. These results mean that Cr^{3+} ions are located in the intermediate ligand field, and energy separation between 2E and ${}^4T_{2g}$ excited levels is not significant. The Dq/B parameter is slightly higher, around 2.41–2.43 for CAZn analogs. The calculated values of Dq/B are similar to those reported recently for DMANaCr (2.29) [15]. However, for some EA and DMA analogs (EANaCr 2.18 [7], EANaAlCr 2.21 [7], DMAKCr 2.21 [37], EAKCr 2.21 [37]) reported Dq/B values are much lower than for the investigated perovskites. On the other hand, the formate perovskites with AM^+ cation comprising Cr^{3+} ions exhibit a strong crystal field (AMNaCr 2.743 [38], AMNaAlCr 2.55 [38]).

The emission spectra of investigated hybrid organic–inorganic formates $[GA]M_{1-x}Cr_x(HCOO)_3$ ($M = Mg^{2+}$, Mn^{2+} , Zn^{2+} , and $x = 0.01, 0.03, 0.05$) recorded at 80 K consists of the intense and narrow emission lines of Cr^{3+} ions located at 686 nm and 698 nm attributed to the spin-forbidden ${}^2E \rightarrow {}^4A_{2g}$ transitions (Figure 5). The broad emission band, which spans from 700 nm to 1000 nm, assigned to the spin-allowed transition from the ${}^4T_{2g}$ excited level to the ${}^4A_{2g}$ ground state is also observed [11,13,16,39]. As can be seen in Figures 5b,d and S5–S7, the emission intensity of GAMg and GAMn samples increased

with the concentration of dopant ions, while the intensity of 1% Cr³⁺ and 5% Cr³⁺ in the GAZn analog are comparable. The samples with 3% of Cr³⁺ are out of the trend. However, the nature of this behavior is unspecified. The collation of the representative samples [GA]M_{1-x}Cr_x(HCOO)₃ (M = Mg²⁺, Mn²⁺, Zn²⁺, and x = 0.05) showed that the most intense luminescence exhibits a sample comprising Mg²⁺ ions. The emission intensity of Mn²⁺ and Zn²⁺ samples is significantly less. The substitution of different metal M²⁺ ions in the crystal structure of guanidine formate have an impact on the intensity relationships between spin-forbidden and spin-allowed transition of Cr³⁺ ions. Only for the GAMg compound ²E → ⁴A_{2g} is emission more intense than spin-allowed transition; for GAMn and GAZn analogs, ⁴T_{2g} → ⁴A_{2g} transition dominates. It is worth noting that no emission of Mn²⁺ ions was detected, probably due to energy reabsorption by chromium ions.

Table 1. The collation of crystal field parameters and energies of electron transitions of the investigated series of [GA]M_{1-x}Cr_x(HCOO)₃ (M = Mg²⁺, Mn²⁺, Zn²⁺, and x = 0.01, 0.03, 0.05).

Parameters	GAMn:			GAMg:			GAZn:		
	1%Cr ³⁺	3%Cr ³⁺	5%Cr ³⁺	1%Cr ³⁺	3%Cr ³⁺	5%Cr ³⁺	1%Cr ³⁺	3%Cr ³⁺	5%Cr ³⁺
⁴ A _{2g} - ² E (cm ⁻¹)	14,535	14,536	14,537	14,552	14,552	14,547	14,540	14,539	14,540
⁴ A _{2g} - ⁴ T _{2g} (cm ⁻¹)	15,545	15,959	15,735	15,828	15,917	16,259	15,640	15,544	15,500
⁴ A _{2g} - ⁴ T _{1g} (cm ⁻¹)	21,972	22,156	22,439	22,703	22,682	22,952	22,062	21,901	21,869
Dq (cm ⁻¹)	1555	1555	1574	1583	1592	1626	1564	1554	1550
B (cm ⁻¹)	650	675	686	709	692	676	648	641	643
Dq/B	2.39	2.30	2.29	2.23	2.30	2.41	2.41	2.43	2.41
C (cm ⁻¹)	3242	3190	3166	3122	3157	3184	3247	3264	3259
C/B	4.13	4.25	4.62	4.40	4.57	4.71	5.01	5.09	5.07

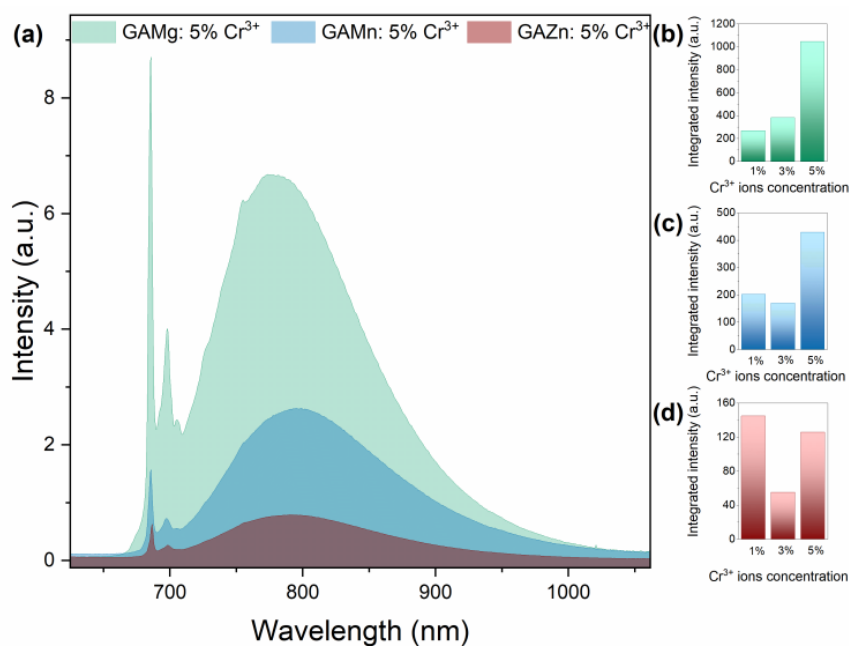


Figure 5. Emission spectra of [GA]M_{1-x}Cr_x(HCOO)₃ (M = Mg²⁺, Mn²⁺, Zn²⁺, and x = 0.05) at 80 K (a) and influence of Cr³⁺ ions concentration of emission intensity (b–d) of the investigated samples.

The emission spectra in the function of temperature were recorded within the range of 80–300 K with 10 K steps. As can be seen in Figures 6 and S8, the main component

of the photoluminescence spectra belongs to the spin-allowed transitions of Cr^{3+} ions. Only for the GAMg sample containing 1% dopant, the ${}^2\text{E}$ emission is much more intense than the band located at 795 nm. Generally, ${}^2\text{E} \rightarrow {}^4\text{A}_{2g}$ emission quenches significantly with increasing temperature, while the ${}^4\text{T}_{2g} \rightarrow {}^4\text{A}_{2g}$ emission of Cr^{3+} is more stable. It is due to the thermally stimulated energy transfer from ${}^2\text{E}$ to ${}^4\text{T}_{2g}$ energy level. Obtained results confirmed the occurrence of the intermediate ligand field in the nearest environment of Cr^{3+} ions. The mechanism of Cr^{3+} luminescence quenching is a well-known phenomenon in the literature and assumes crossing the ${}^4\text{T}_{2g}$ excited state parabola with the ${}^4\text{A}_{2g}$ one [11,13,16,39].

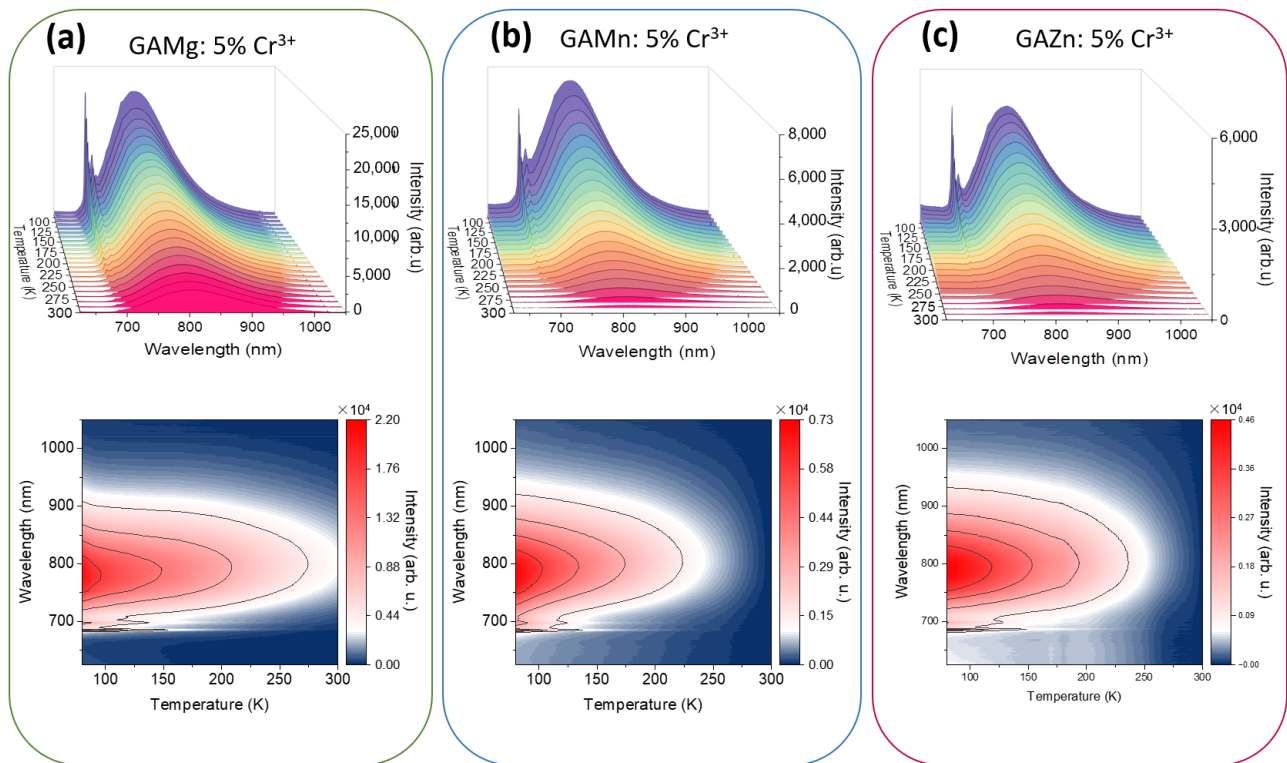


Figure 6. Temperature-dependent emission spectra and thermal evolution of emission intensity of $[\text{GA}]\text{Mg}(\text{HCOO})_3: 5\% \text{Cr}^{3+}$ (a), $[\text{GA}]\text{Mn}(\text{HCOO})_3: 5\% \text{Cr}^{3+}$ (b), and $[\text{GA}]\text{Zn}(\text{HCOO})_3: 5\% \text{Cr}^{3+}$ (c) representative samples, respectively.

The significant dependence of photoluminescence intensity on temperature may be an interesting behavior that can be exploited for non-contact temperature readout based on luminescence. Figure 7 demonstrates a schematic representation of the approach to temperature determination. In this model, the Fluorescence Intensity Ratio (FIR) parameter can be defined as a ratio of the ${}^2\text{E} \rightarrow {}^4\text{A}_{2g}$ (spectral range 670–710 nm marked as I_1) to the ${}^4\text{T}_{2g} \rightarrow {}^4\text{A}_{2g}$ (spectral range 750–1050 nm represented as I_2) transition of Cr^{3+} ions, respectively.

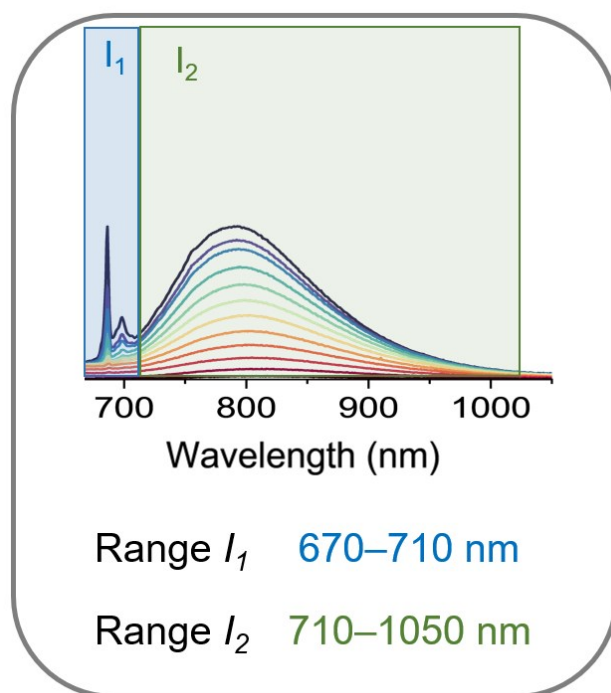


Figure 7. Graphical representation of way for the temperature detection in hybrid organic–inorganic formate perovskites $[GA]M_{1-x}Cr_x(HCOO)_3$ ($M = Mg^{2+}, Mn^{2+}, Zn^{2+}$, and $x = 0.01, 0.03, 0.05$).

The proposed model was tested on the investigated $[GA]M_{1-x}Cr_x(HCOO)_3$ ($M = Mg^{2+}, Mn^{2+}, Zn^{2+}$, and $x = 0.01, 0.03, 0.05$) hybrid organic–inorganic perovskites. It is clear that the increase in temperature causes decreasing in FIR (Figure 8), and the highest value of FIR was obtained for the GAMg: 1% Cr^{3+} sample. To further comparison of the observed changes in thermometric parameters and to compare their features, the absolute (S_a) and relative (S_r) sensitivities were calculated as follows:

$$S_a = \left| \frac{dFIR}{dT} \right| \quad (1)$$

and

$$S_r = \frac{1}{FIR} \left| \frac{dFIR}{dT} \right| \quad (2)$$

where $dFIR$ represents the change of fluorescence intensity ratio at temperature change ΔT . The collation of S_a and S_r changes of the investigated hybrid organic–inorganic perovskites are presented in Figures 9 and S9. Generally, the S_a and S_r values are the highest at the 80–120 K range and decrease with increasing temperature. However, the sensitivity changes with sample composition and concentration of Cr^{3+} ions. For GAMg: Cr^{3+} compounds, the significant relative sensitivity exhibits sample with the lowest concentration of dopant ions and equals $2.08\%K^{-1}$ at 90 K. With increasing Cr^{3+} ions concentration, the S_r decreased to around $1\%K^{-1}$. Substitution of Mg^{2+} by Mn^{2+} caused a decrease of sensitivity to $1.20\%K^{-1}$, but the optimal Cr^{3+} ions concentration was determined to be 3%. Similar trends are observed for GAZn: for Cr^{3+} analogs, however, the changes of S_r with chromium ions concentration are negligible, and the highest S_r is $1.08\%K^{-1}$ at 90 K for GAZn: 1% Cr^{3+} . Additionally, the repeatability of the thermal sensing performance of representative samples was verified by the circling heat/cool process (Figure S10). It can be seen that only a small variation from the initial value was observed, and the temperature parameter Δ is reversed and repeated overheating/cooling cycles.

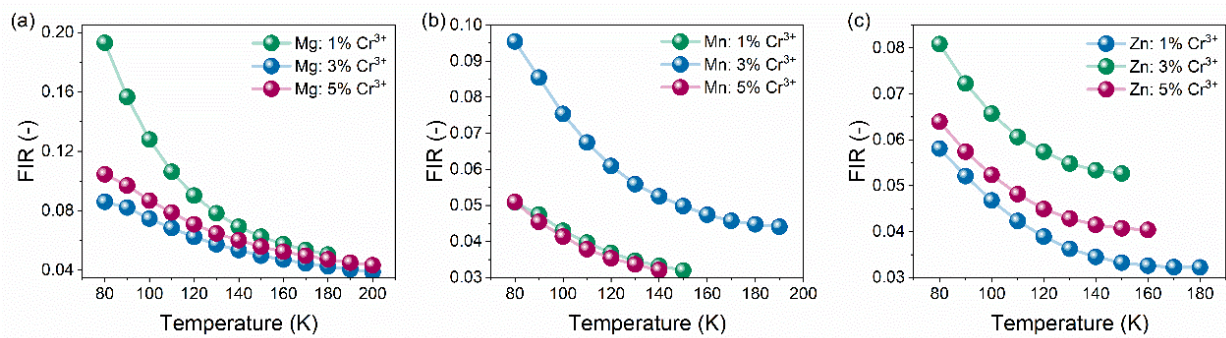


Figure 8. Influence of Cr^{3+} ions concentration on Fluorescence Intensity Ratio (FIR) (a–c) of $[\text{GA}]\text{M}_{1-x}\text{Cr}_x(\text{HCOO})_3$ ($\text{M} = \text{Mg}^{2+}, \text{Mn}^{2+}, \text{Zn}^{2+}$, and $x = 0.01, 0.03, 0.05$) hybrid perovskites.

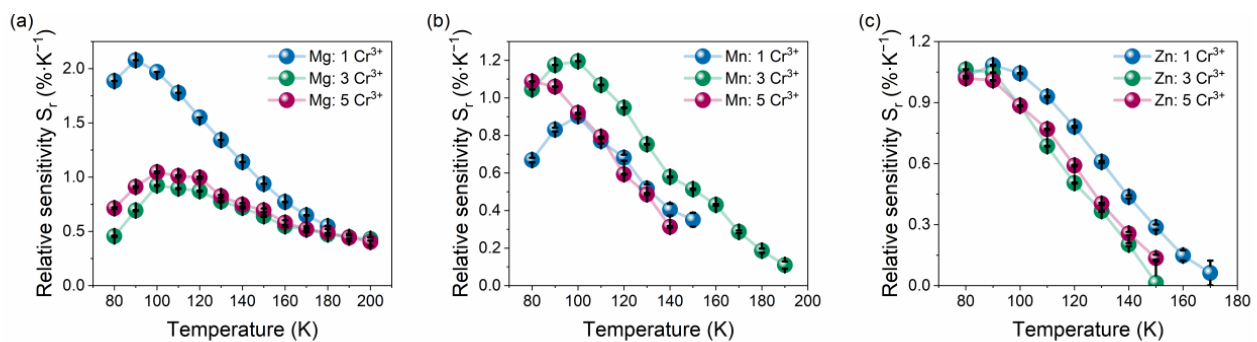


Figure 9. Influence of Cr^{3+} ions concentration on relative sensitivity S_r (a–c) of $[\text{GA}]\text{M}_{1-x}\text{Cr}_x(\text{HCOO})_3$ ($\text{M} = \text{Mg}^{2+}, \text{Mn}^{2+}, \text{Zn}^{2+}$, and $x = 0.01, 0.03, 0.05$) hybrid perovskites.

In fact, only one optical thermometer based on hybrid organic–inorganic formate perovskites $[\text{EA}]_2\text{NaCr}_{0.21}\text{Al}_{0.79}(\text{HCOO})_6$ with a sensitivity S_r of $2.84\% \text{K}^{-1}$ at 160 K is known [10]. Obtained values of relative sensitivities were compared with the S_r values of other inorganic and hybrid organic–inorganic luminescent thermometers (Table 2). The results show that investigated $[\text{GA}]\text{M}_{1-x}\text{Cr}_x(\text{HCOO})_3$ ($\text{M} = \text{Mg}^{2+}, \text{Mn}^{2+}, \text{Zn}^{2+}$, and $x = 0.01, 0.03, 0.05$) has the potential to be applied as a low-temperature luminescent thermometer.

Table 2. Collation of exemplary luminescent thermometers with their highest relative sensitivity (S_r) at working temperature (T)¹.

Compound	S_r ($\% \text{K}^{-1}$)	T (K)	Reference
$[\text{GA}]\text{Mg}(\text{HCOO})_3: 1\% \text{Cr}^{3+}$	2.08	90	This work
$[\text{GA}]\text{Zn}(\text{HCOO})_3: 1\% \text{Cr}^{3+}$	1.08	90	This work
$[\text{GA}]\text{Mn}(\text{HCOO})_3: 3\% \text{Cr}^{3+}$	1.20	100	This work
$[\text{EA}]_2\text{NaCr}_{0.21}\text{Al}_{0.79}(\text{HCOO})_6$	2.84	160	[10]
$(\text{Me}_2\text{NH}_2)_3[\text{Eu}_3(\text{FDC})_4(\text{NO}_3)_4] \cdot 4\text{H}_2\text{O}$	2.7	170	[40]
$\text{Sr}(\text{HCOO})_2:\text{Eu}^{2+}/\text{Eu}^{3+}$	3.8	293	[41]
Ln-cpda (Ln = Eu, Tb)	16	300	[42]
TbMOF@3%Eu-tfac	2.59	225	[43]
$[\text{Eu}_2(\text{qptca})(\text{NO}_3)_2(\text{DMF})_4](\text{CH}_3\text{CH}_2\text{OH})_3$ perylene	1.28	293	[44]
$\text{Bi}_2\text{Ga}_4\text{O}_9:\text{Cr}^{3+}$	0.7	290	[45]
$\text{Bi}_2\text{Al}_4\text{O}_9:\text{Cr}^{3+}$	1.24	290	[46]

Table 2. Cont.

Compound	S_r (%K ⁻¹)	T (K)	Reference
Sr ₂ MgAl ₂₂ O ₃₆ :Cr ³⁺	1.7	310	[47]
ZnGa ₂ O ₄ :Cr ³⁺	2.8	310	[48]
SrAl ₁₂ O ₁₉ :Mn ⁴⁺	0.27	393	[49]
LaPO ₄ :Nd ³⁺	7.19	303	[50]
MgTiO ₃ :Mn ⁴⁺	1.2	93	[51]
La ₂ MgTiO ₆ : Cr ³⁺ , V ⁴⁺	1.96	165	[11]

¹ GA—guanidine, EA—ethylammonium, H₂FDC—9-fluorenone-2,7-dicarboxylic acid, H₃cpda—5-(4-carboxyphenyl)-2,6-pyridinedicarboxylic acid, TbMOF—[Tb₂(bpydc)₃(H₂O)₃]*n*DMF, H₂bpydc—2,2-bipyridine-5,5'-dicarboxylic acid, tfac—trifluoroacetylacetonate, H₄qptca—1,1':4',1'':4'',1''':4'''-quaterphenyl-3,3''',5,5'''-tetracarboxylic acid, DMF—dimethylformamide.

4. Conclusions

Three series of samples [C(NH₂)₃]M(HCOO)₃ (Mg²⁺, Mn²⁺, Zn²⁺) doped with 1%, 3%, and 5% of Cr³⁺ ions were synthesized using the low-diffusion synthesis method. Their structural, phonon, and luminescent properties were investigated in detail. It was shown that the incorporation of Cr³⁺ ions into the crystal structure of investigated hybrid organic-inorganic perovskites does not affect the phase purity of the samples. Based on diffuse reflectance spectra, crystal field strength (Dq/B) and Racah parameters were determined. It was found that Cr³⁺ ions are located in the intermediate crystal field or close to it with a Dq/B range of 2.29–2.41. The investigation of sample composition showed that the highest emission intensity exhibits GAMg: 5% Cr³⁺ sample, while the lowest one GAZn: 5% Cr³⁺. The presence of both the spin-forbidden and spin-allowed transitions of Cr³⁺ ions at a broad temperature range enables the characterization of these materials as luminescence thermometers. It turned out that the relative sensitivity of S_r depends on the sample composition and concentration of Cr³⁺ ions. The highest relative sensitivity $S_r = 2.08\%K^{-1}$ at 90 K has [GA]Mg(HCOO)₃: 1% Cr³⁺. Replacement of Mg²⁺ by Mn²⁺ or Zn²⁺ reduced the sensitivity to 1.20%K⁻¹ at 100 K and 1.08%K⁻¹ at 90 K for [GA]Mn(HCOO)₃: 3% Cr³⁺ and [GA]Zn(HCOO)₃: 1% Cr³⁺, respectively.

Supplementary Materials: The following supporting information can be downloaded at: <https://www.mdpi.com/article/10.3390/s23146259/s1>, Figure S1. Diffuse reflectance spectra of a series of [GA]Mn_{1-x}Cr_x(HCOO)₃ (x = 0, 0.01, 0.03, 0.05) measured at 300 K.; Figure S2. Diffuse reflectance spectra of a series of [GA]Mg_{1-x}Cr_x(HCOO)₃ (x = 0, 0.01, 0.03, 0.05) measured at 300 K.; Figure S3. Diffuse reflectance spectra of a series of [GA]Zn_{1-x}Cr_x(HCOO)₃ (x = 0, 0.01, 0.03, 0.05) measured at 300 K.; Figure S4. Deconvolution of the absorption spectrum of [GA]Mn_{1-x}Cr_x(HCOO)₃ (x = 0.05) measured at 300 K.; Figure S5. Low-temperature emission spectra of [GA]Mg_{1-x}Cr_x(HCOO)₃ (x = 0.01, 0.03, 0.05).; Figure S6. Low-temperature emission spectra of [GA]Mn_{1-x}Cr_x(HCOO)₃ (x = 0.01, 0.03, 0.05).; Figure S7. Low-temperature emission spectra of [GA]Zn_{1-x}Cr_x(HCOO)₃ (x = 0.01, 0.03, 0.05).; Figure S8. Temperature-dependent emission spectra of [GA]Mn_{1-x}Cr_x(HCOO)₃ x = 0.01 (a), [GA]Mn_{1-x}Cr_x(HCOO)₃ x = 0.03 (b), [GA]Mg_{1-x}Cr_x(HCOO)₃ x = 0.01 (c), [GA]Mg_{1-x}Cr_x(HCOO)₃ x = 0.03 (d), [GA]Zn_{1-x}Cr_x(HCOO)₃ x = 0.01 (e), and [GA]Zn_{1-x}Cr_x(HCOO)₃ x = 0.03 (f) samples.; Figure S9. Influence of Cr³⁺ ions concentration on absolute sensitivity (S_a) (a–c) of [GA]M_{1-x}Cr_x(HCOO)₃ (M = Mg²⁺, Mn²⁺, Zn²⁺, and x = 0.01, 0.03, 0.05) hybrid perovskites.; Figure S10. Repeatability of Δ temperature parameter of I₁/I₂ emission evaluated at 80 K and 100 K during 10 heating/cooling cycles of (a) [GA]Mg_{1-x}Cr_x(HCOO)₃ x = 0.01, (b) [GA]Mn_{1-x}Cr_x(HCOO)₃ x = 0.03, and (c) [GA]Zn_{1-x}Cr_x(HCOO)₃ x = 0.01.; Table S1. Quantities of precursors used for the syntheses of the series of [GA]Mn_{1-x}Cr_x(HCOO)₃.; Table S2. Quantities of precursors used for the syntheses of the series of [GA]Mg_{1-x}Cr_x(HCOO)₃.; Table S3. Quantities of precursors used for the syntheses of the series of [GA]Zn_{1-x}Cr_x(HCOO)₃.; Table S4. Lattice parameters and calculated factors (d_{oct} , average M^{II}–O bond length; V_{oct} , M^{II}O₆ octahedral volume; σ^2 , bond angle variance; Δ , distortion index) [10.1107/S0021889811038970] for [GA]Mn(HCOO)₃ and

[GA]Zn(HCOO)₃ based on the crystal data published in [10.1002/chem.200901605].; Determination of δT . References [25,52,53] are cited in Supplementary Materials.

Author Contributions: Conceptualization, D.S.; methodology, D.S.; validation, D.S.; formal analysis, D.S., A.K., T.H.Q.V., M.A. and M.P.; investigation, D.S., A.K., T.H.Q.V., M.A. and M.P.; data curation, D.S., M.A. and M.P.; writing—original draft preparation, D.S., A.K., T.H.Q.V., M.A. and M.P.; writing—review and editing, D.S., A.K., T.H.Q.V., M.A. and M.P.; visualization, D.S., A.K., T.H.Q.V., M.A. and M.P.; supervision, D.S.; project administration, D.S.; funding acquisition, D.S. All authors have read and agreed to the published version of the manuscript.

Funding: This research was funded in whole by the National Science Centre, Poland, under project no. UMO-2020/39/D/ST5/01289. For the purpose of open access, the author has applied for a CC-BY public copyright license to any Author Accepted Manuscript (AAM) version arising from this submission.

Data Availability Statement: Experimental data: The Raman and diffuse reflectance spectra, temperature-dependent luminescence and emission maps, thermometric parameters, powder XRD data, and low-temperature emission spectra are available at 10.5281/zenodo.7970355.

Acknowledgments: The authors would also like to thank E. Bukowska for the XRD measurements and B. Macalik for the absorption measurements.

Conflicts of Interest: The authors declare no conflict of interest.

References

1. Ptak, M.; Sieradzki, A.; Šimėnas, M.; Maczka, M. Molecular Spectroscopy of Hybrid Organic–Inorganic Perovskites and Related Compounds. *Coord. Chem. Rev.* **2021**, *448*, 214180. [\[CrossRef\]](#)
2. Ptak, M.; Zarychta, B.; Stefańska, D.; Ciupa, A.; Paraguassu, W. Novel Bimetallic MOF Phosphors with an Imidazolium Cation: Structure, Phonons, High- Pressure Phase Transitions and Optical Response. *Dalt. Trans.* **2019**, *48*, 242–252. [\[CrossRef\]](#) [\[PubMed\]](#)
3. Drozdowski, D.; Fedoruk, K.; Kabański, A.; Maczka, M.; Sieradzki, A.; Gaĝor, A. Broadband Yellow and White Emission from Large Octahedral Tilting in (110)-Oriented Layered Perovskites: Imidazolium-Methylhydrazinium Lead Halides. *J. Mater. Chem. C* **2023**, *11*, 4907–4915. [\[CrossRef\]](#)
4. Prochowicz, D.; Frankevičius, M.; Cieślak, A.M.; Zakeeruddin, S.M.; Grätzel, M.; Lewiński, J. Mechanochemical Synthesis of the Hybrid Perovskite CH₃NH₃PbI₃: Characterization and the Corresponding Solar Cell Efficiency. *J. Mater. Chem. A* **2015**, *3*, 20772–20777. [\[CrossRef\]](#)
5. Marimuthu, T.; Yuvakkumar, R.; Kumar, P.S.; Vo, D.V.N.; Xu, X.; Xu, G. Two-Dimensional Hybrid Perovskite Solar Cells: A Review. *Environ. Chem. Lett.* **2022**, *20*, 189–210. [\[CrossRef\]](#)
6. Kim, J.Y.; Lee, J.W.; Jung, H.S.; Shin, H.; Park, N.G. High-Efficiency Perovskite Solar Cells. *Chem. Rev.* **2020**, *120*, 7867–7918. [\[CrossRef\]](#) [\[PubMed\]](#)
7. Ptak, M.; Maczka, M.; Gaĝor, A.; Sieradzki, A.; Bondzior, B.; Dereń, P.; Pawlus, S. Phase Transitions and Chromium(III) Luminescence in Perovskite-Type [C₂H₅NH₃][Na_{0.5}Cr_xAl_{0.5-x}(HCOO)₃] (x = 0, 0.025, 0.5), Correlated with Structural, Dielectric and Phonon Properties. *Phys. Chem. Chem. Phys.* **2016**, *18*, 29629–29640. [\[CrossRef\]](#)
8. Huang, C.R.; Luo, X.; Chen, X.G.; Song, X.J.; Zhang, Z.X.; Xiong, R.G. A Multiaxial Lead-Free Two-Dimensional Organic-Inorganic Perovskite Ferroelectric. *Natl. Sci. Rev.* **2021**, *8*, nwa232. [\[CrossRef\]](#)
9. Wang, Z.C.; Rogers, J.D.; Yao, X.; Nichols, R.; Atay, K.; Xu, B.; Franklin, J.; Sochnikov, I.; Ryan, P.J.; Haskel, D.; et al. Colossal Magnetoresistance without Mixed Valence in a Layered Phosphide Crystal. *Adv. Mater.* **2021**, *33*, 2005755. [\[CrossRef\]](#)
10. Kabański, A.; Ptak, M.; Stefańska, D. Metal-Organic Framework Optical Thermometer Based on Cr³⁺ Ion Luminescence. *ACS Appl. Mater. Interfaces* **2023**, *15*, 7074–7082. [\[CrossRef\]](#)
11. Stefańska, D.; Bondzior, B.; Vu, T.H.Q.; Grodzicki, M.; Dereń, P.J. Temperature Sensitivity Modulation through Changing the Vanadium Concentration in a La₂MgTiO₆:V⁵⁺, Cr³⁺ double Perovskite Optical Thermometer. *Dalt. Trans.* **2021**, *50*, 9851–9857. [\[CrossRef\]](#)
12. Wu, Y.; Fan, W.; Gao, Z.; Tang, Z.; Lei, L.; Sun, X.; Li, Y.; Cai, H.L.; Wu, X. New Photoluminescence Hybrid Perovskites with Ultrahigh Photoluminescence Quantum Yield and Ultrahigh Thermostability Temperature up to 600 K. *Nano Energy* **2020**, *77*, 105170. [\[CrossRef\]](#)
13. Stefańska, D.; Vu, T.H.Q.; Dereń, P.J. Multiple Ways for Temperature Detection Based on La₂MgTiO₆ Double Perovskite Co-Doped with Mn⁴⁺ and Cr³⁺ Ions. *J. Alloys Compd.* **2023**, *938*, 22–26. [\[CrossRef\]](#)
14. Ptak, M.; Dziuk, B.; Stefańska, D.; Hermanowicz, K. The Structural, Phonon and Optical Properties of [CH₃NH₃][M_{0.5}Cr_xAl_{0.5-x}(HCOO)₃] (M = Na, K; X = 0, 0.025, 0.5) Metal-Organic Framework Perovskites for Luminescence Thermometry. *Phys. Chem. Chem. Phys.* **2019**, *21*, 7965–7972. [\[CrossRef\]](#)

15. Mączka, M.; Bondzior, B.; Dereń, P.; Sieradzki, A.; Trzmiel, J.; Pietraszko, A.; Hanuza, J. Synthesis and Characterization of $[(\text{CH}_3)_2\text{NH}_2][\text{Na}_{0.5}\text{Cr}_{0.5}(\text{HCOO})_3]$: A Rare Example of Luminescent Metal-Organic Frameworks Based on Cr(III) Ions. *Dalt. Trans.* **2015**, *44*, 6871–6879. [[CrossRef](#)] [[PubMed](#)]
16. Dereń, P.J.; Malinowski, M.; Stręk, W. Site Selection Spectroscopy of Cr^{3+} in MgAl_2O_4 Green Spinel. *J. Lumin.* **1996**, *68*, 91–103. [[CrossRef](#)]
17. Lin, H.; Bai, G.; Yu, T.; Tsang, M.K.; Zhang, Q.; Hao, J. Site Occupancy and Near-Infrared Luminescence in $\text{Ca}_3\text{Ga}_2\text{Ge}_3\text{O}_{12}$: Cr^{3+} Persistent Phosphor. *Adv. Opt. Mater.* **2017**, *5*, 1700227. [[CrossRef](#)]
18. Bolek, P.; Zeler, J.; Carlos, L.D.; Zych, E. Mixing Phosphors to Improve the Temperature Measuring Quality. *Opt. Mater.* **2021**, *122*, 111719. [[CrossRef](#)]
19. Yin, H.Q.; Yin, X.B. Metal-Organic Frameworks with Multiple Luminescence Emissions: Designs and Applications. *Acc. Chem. Res.* **2020**, *53*, 485–495. [[CrossRef](#)]
20. Maturi, F.E.; Brites, C.D.S.; Ximendes, E.C.; Mills, C.; Olsen, B.; Jaque, D.; Ribeiro, S.J.L.; Carlos, L.D. Going Above and Beyond: A Tenfold Gain in the Performance of Luminescence Thermometers Joining Multiparametric Sensing and Multiple Regression. *Laser Photonics Rev.* **2021**, *15*, 2100301. [[CrossRef](#)]
21. Sójka, M.; Brites, C.D.S.; Carlos, L.D.; Zych, E. Exploiting Bandgap Engineering to Finely Control Dual-Mode $\text{Lu}_2(\text{Ge,Si})\text{O}_5:\text{Pr}^{3+}$ luminescence Thermometers. *J. Mater. Chem. C* **2020**, *8*, 10086–10097. [[CrossRef](#)]
22. Sójka, M.; Runowski, M.; Zheng, T.; Shyichuk, A.; Kulesza, D.; Zych, E.; Lis, S. Eu^{2+} emission from Thermally Coupled Levels—New Frontiers for Ultrasensitive Luminescence Thermometry. *J. Mater. Chem. C* **2022**, *10*, 1220–1227. [[CrossRef](#)]
23. del Rosal, B.; Ximendes, E.; Rocha, U.; Jaque, D. In Vivo Luminescence Nanothermometry: From Materials to Applications. *Adv. Opt. Mater.* **2017**, *5*, 1600508. [[CrossRef](#)]
24. Marciniak, L.; Bednarkiewicz, A. Nanocrystalline NIR-to-NIR Luminescent Thermometer Based on $\text{Cr}^{3+}, \text{Yb}^{3+}$ Emission. *Sens. Actuators B Chem.* **2017**, *243*, 388–393. [[CrossRef](#)]
25. Brites, C.D.S.; Millán, A.; Carlos, L.D. Lanthanides in Luminescent Thermometry. *Handb. Phys. Chem. Rare Earths* **2016**, *49*, 339–427. [[CrossRef](#)]
26. Łukaszewicz, M.; Tomala, R.; Lisiecki, R. From Upconversion to Thermal Radiation: Spectroscopic Properties of a Submicron $\text{Y}_2\text{O}_3:\text{Er}^{3+}, \text{Yb}^{3+}$ Ceramic under IR Excitation in an Extremely Broad Temperature Range. *J. Mater. Chem. C* **2020**, *8*, 1072–1082. [[CrossRef](#)]
27. Gavrilović, T.V.; Jovanović, D.J.; Lojpur, V.; Dramićanin, M.D. Multifunctional Eu^{3+} - and $\text{Er}^{3+}/\text{Yb}^{3+}$ -Doped GdVO_4 Nanoparticles Synthesized by Reverse Micelle Method. *Sci. Rep.* **2014**, *4*, 4209. [[CrossRef](#)]
28. Łukaszewicz, M.; Klimesz, B.; Szmalenberg, A.; Ptak, M.; Lisiecki, R. Neodymium-Doped Germanotellurite Glasses for Laser Materials and Temperature Sensing. *J. Alloys Compd.* **2021**, *860*, 157923. [[CrossRef](#)]
29. Piotrowski, W.; Kniec, K.; Marciniak, L. Enhancement of the Ln^{3+} Ratiometric Nanothermometers by Sensitization with Transition Metal Ions. *J. Alloys Compd.* **2021**, *870*, 159386. [[CrossRef](#)]
30. Marciniak, L.; Kniec, K.; Elźbięciak-Piecka, K.; Trejgis, K.; Stefanska, J.; Dramićanin, M. Luminescence Thermometry with Transition Metal Ions. A Review. *Coord. Chem. Rev.* **2022**, *469*, 214671. [[CrossRef](#)]
31. Hu, K.L.; Kurmoo, M.; Wang, Z.; Gao, S. Metal-Organic Perovskites: Synthesis, Structures, and Magnetic Properties of $[\text{C}(\text{NH}_2)_3][\text{M}^{\text{II}}(\text{HCOO})_3]$ ($\text{M} = \text{Mn, Fe, Co, Ni, Cu, and Zn}$; $\text{C}(\text{NH}_2)_3 = \text{guanidinium}$). *Chem.—A Eur. J.* **2009**, *15*, 12050–12064. [[CrossRef](#)] [[PubMed](#)]
32. Shannon, R.D. Revised Effective Ionic Radii and Systematic Studies of Interatomic Distances in Halides and Chalcogenides. *Acta Crystallogr. Sect. A* **1976**, *32*, 751–767. [[CrossRef](#)]
33. Gui, D.; Ji, L.; Muhammad, A.; Li, W.; Cai, W.; Li, Y.; Li, X.; Wu, X.; Lu, P. Jahn-Teller Effect on Framework Flexibility of Hybrid Organic-Inorganic Perovskites. *J. Phys. Chem. Lett.* **2018**, *9*, 751–755. [[CrossRef](#)]
34. Collings, I.E.; Hill, J.A.; Cairns, A.B.; Cooper, R.I.; Thompson, A.L.; Parker, J.E.; Tang, C.C.; Goodwin, A.L. Compositional Dependence of Anomalous Thermal Expansion in Perovskite-like ABX_3 Formates. *Dalt. Trans.* **2016**, *45*, 4169–4178. [[CrossRef](#)]
35. Rossin, A.; Chierotti, M.R.; Giambastiani, G.; Gobetto, R.; Peruzzini, M. Amine-Templated Polymeric Mg Formates: Crystalline Scaffolds Exhibiting Extensive Hydrogen Bonding. *CrystEngComm* **2012**, *14*, 4454–4460. [[CrossRef](#)]
36. Mączka, M.; Ptak, M.; Macalik, L. Infrared and Raman Studies of Phase Transitions in Metal-Organic Frameworks of $[(\text{CH}_3)_2\text{NH}_2][\text{M}(\text{HCOO})_3]$ with $\text{M} = \text{Zn, Fe}$. *Vib. Spectrosc.* **2014**, *71*, 98–104. [[CrossRef](#)]
37. Ptak, M.; Gagor, A.; Sieradzki, A.; Bondzior, B.; Dereń, P.; Ciupa, A.; Trzebiatowska, M.; Mączka, M. The Effect of K^+ Cations on the Phase Transitions, and Structural, Dielectric and Luminescence Properties of $[\text{Cat}][\text{K}_{0.5}\text{Cr}_{0.5}(\text{HCOO})_3]$, Where Cat Is Protonated Dimethylamine or Ethylamine. *Phys. Chem. Chem. Phys.* **2017**, *19*, 12156–12166. [[CrossRef](#)]
38. Ptak, M.; Stefańska, D.; Gagor, A.; Svane, K.L.; Walsh, A.; Paraguassu, W. Heterometallic Perovskite-Type Metal-Organic Framework with an Ammonium Cation: Structure, Phonons, and Optical Response of $[\text{NH}_4][\text{Na}_{0.5}\text{Cr}_x\text{Al}_{0.5-x}(\text{HCOO})_3]$ ($x = 0, 0.025$ and 0.5). *Phys. Chem. Chem. Phys.* **2018**, *20*, 22284–22295. [[CrossRef](#)]
39. Mikenda, W.; Preisinger, A. N-Lines in the Luminescence Spectra of Cr^{3+} -Doped Spinel (II) Origins of N-Lines. *J. Lumin.* **1981**, *26*, 67–83. [[CrossRef](#)]
40. Li, L.; Zhu, Y.; Zhou, X.; Brites, C.D.S.; Ananias, D.; Lin, Z.; Paz, F.A.A.; Rocha, J.; Huang, W.; Carlos, L.D. Visible-Light Excited Luminescent Thermometer Based on Single Lanthanide Organic Frameworks. *Adv. Funct. Mater.* **2016**, *26*, 8677–8684. [[CrossRef](#)]

41. Liu, W.; Liu, L.; Wang, Y.; Chen, L.; McLeod, J.A.; Yang, L.; Zhao, J.; Liu, Z.; Diwu, J.; Chai, Z.; et al. Tuning Mixed-Valent $\text{Eu}^{2+}/\text{Eu}^{3+}$ in Strontium Formate Frameworks for Multichannel Photoluminescence. *Chemistry* **2016**, *22*, 11170–11175. [[CrossRef](#)] [[PubMed](#)]
42. Paquin, F.; Rivnay, J.; Salleo, A.; Stingelin, N.; Silva, C. Multi-Phase Semicrystalline Microstructures Drive Exciton Dissociation in Neat Plastic Semiconductors. *J. Mater. Chem. C* **2015**, *3*, 10715–10722. [[CrossRef](#)]
43. Kaczmarek, A.M.; Liu, Y.Y.; Wang, C.; Laforce, B.; Vincze, L.; Van Der Voort, P.; Van Deun, R. Grafting of a Eu^{3+} -Tfac Complex on to a Tb^{3+} -Metal Organic Framework for Use as a Ratiometric Thermometer. *Dalt. Trans.* **2017**, *46*, 12717–12723. [[CrossRef](#)] [[PubMed](#)]
44. Cui, Y.; Song, R.; Yu, J.; Liu, M.; Wang, Z.; Wu, C.; Yang, Y.; Wang, Z.; Chen, B.; Qian, G. Dual-Emitting MOF \cap dye Composite for Ratiometric Temperature Sensing. *Adv. Mater.* **2015**, *27*, 1420–1425. [[CrossRef](#)] [[PubMed](#)]
45. Back, M.; Trave, E.; Ueda, J.; Tanabe, S. Ratiometric Optical Thermometer Based on Dual Near-Infrared Emission in Cr^{3+} -Doped Bismuth-Based Gallate Host. *Chem. Mater.* **2016**, *28*, 8347–8356. [[CrossRef](#)]
46. Back, M.; Ueda, J.; Xu, J.; Asami, K.; Brik, M.G.; Tanabe, S. Effective Ratiometric Luminescent Thermal Sensor by Cr^{3+} -Doped Mullite $\text{Bi}_2\text{Al}_4\text{O}_9$ with Robust and Reliable Performances. *Adv. Opt. Mater.* **2020**, *8*, 2000124. [[CrossRef](#)]
47. Wang, Q.; Liang, Z.; Luo, J.; Yang, Y.; Mu, Z.; Zhang, X.; Dong, H.; Wu, F. Ratiometric Optical Thermometer with High Sensitivity Based on Dual Far-Red Emission of Cr^{3+} in $\text{Sr}_2\text{MgAl}_{22}\text{O}_{36}$. *Ceram. Int.* **2020**, *46*, 5008–5014. [[CrossRef](#)]
48. Ueda, J.; Back, M.; Brik, M.G.; Zhuang, Y.; Grinberg, M.; Tanabe, S. Ratiometric Optical Thermometry Using Deep Red Luminescence from $^4\text{T}_2$ and ^2E States of Cr^{3+} in ZnGa_2O_4 Host. *Opt. Mater.* **2018**, *85*, 510–516. [[CrossRef](#)]
49. Yang, S.H.; Lee, Y.C.; Hung, Y.C. Thermometry of Red Nanoflaked $\text{SrAl}_{12}\text{O}_{19}:\text{Mn}^{4+}$ Synthesized with Boric Acid Flux. *Ceram. Int.* **2018**, *44*, 11665–11673. [[CrossRef](#)]
50. Trejgis, K.; Maciejewska, K.; Bednarkiewicz, A.; Marciniak, L. Near-Infrared-to-Near-Infrared Excited-State Absorption in $\text{LaPO}_4:\text{Nd}^{3+}$ Nanoparticles for Luminescent Nanothermometry. *ACS Appl. Nano Mater.* **2020**, *3*, 4818–4825. [[CrossRef](#)]
51. Glais, E.; Dordević, V.; Papan, J.; Viana, B.; Dramićanin, M.D. $\text{MgTiO}_3:\text{Mn}^{4+}$ a Multi-Reading Temperature Nanoprobe. *RSC Adv.* **2018**, *8*, 18341–18346. [[CrossRef](#)] [[PubMed](#)]
52. Reshchikov, M.A. Mechanisms of Thermal Quenching of Defect-Related Luminescence in Semiconductors. *Phys. Status Solidi A* **2020**, *218*, 2000101. [[CrossRef](#)]
53. Shionoya, S. Photoluminescence. In *Luminescence of Solids*; Springer: Boston, MA, USA, 2021. [[CrossRef](#)]

Disclaimer/Publisher's Note: The statements, opinions and data contained in all publications are solely those of the individual author(s) and contributor(s) and not of MDPI and/or the editor(s). MDPI and/or the editor(s) disclaim responsibility for any injury to people or property resulting from any ideas, methods, instructions or products referred to in the content.